Monthly Notices of the ROYAL ASTRONOMICAL SOCIETY
MNRAS **456,** 2080–2094 (2016) doi:10.1093/mnras/stv2812

Effects of the sources of reionization on 21-cm redshift-space distortions

Suman Majumdar,[1,2⋆] Hannes Jensen,[1,3⋆] Garrelt Mellema,[1] Emma Chapman,[4] Filipe B. Abdalla,[4,5] Kai-Yan Lee,[1] Ilian T. Iliev,[6] Keri L. Dixon,[6] Kanan K. Datta,[7] Benedetta Ciardi,[8] Elizabeth R. Fernandez,[9] Vibor Jelić,[9,10,11] Léon V. E. Koopmans[9] and Saleem Zaroubi[9]

[1]*Department of Astronomy and Oskar Klein Centre, Stockholm University, AlbaNova, SE-10691 Stockholm, Sweden*
[2]*Department of Physics, Blackett Laboratory, Imperial College, London SW7 2AZ, UK*
[3]*Department of Physics and Astronomy, Uppsala University, 75120 Uppsala, Sweden*
[4]*Department of Physics and Astronomy, University College London, Gower Street, London WC1E 6BT, UK*
[5]*Department of Physics and Electronics, Rhodes University, PO Box 94, Grahamstown 6140, South Africa*
[6]*Astronomy Centre, Department of Physics & Astronomy, Pevensey II Building, University of Sussex, Falmer, Brighton BN1 9QH, UK*
[7]*Department of Physics, Presidency University, 86/1 College Street, Kolkata 700073, India*
[8]*Max-Planck-Institut für Astrophysik, Karl-Schwarzschild-Strasse 1, D-85748 Garching b. München, Germany*
[9]*Kapteyn Astronomical Institute, University of Groningen, PO Box 800, NL-9700 AV Groningen, the Netherlands*
[10]*ASTRON – the Netherlands Institute for Radio Astronomy, PO Box 2, NL-7990 AA Dwingeloo, the Netherlands*
[11]*Ruđer Bošković Institute, Bijenička cesta 54, 10000 Zagreb, Croatia*

Accepted 2015 November 27. Received 2015 November 8; in original form 2015 September 24

ABSTRACT

The observed 21 cm signal from the epoch of reionization will be distorted along the line of sight by the peculiar velocities of matter particles. These *redshift-space distortions* will affect the contrast in the signal and will also make it anisotropic. This anisotropy contains information about the cross-correlation between the matter density field and the neutral hydrogen field, and could thus potentially be used to extract information about the sources of reionization. In this paper, we study a collection of simulated reionization scenarios assuming different models for the sources of reionization. We show that the 21 cm anisotropy is best measured by the quadrupole moment of the power spectrum. We find that, unless the properties of the reionization sources are extreme in some way, the quadrupole moment evolves very predictably as a function of global neutral fraction. This predictability implies that redshift-space distortions are not a very sensitive tool for distinguishing between reionization sources. However, the quadrupole moment can be used as a model-independent probe for constraining the reionization history. We show that such measurements can be done to some extent by first-generation instruments such as LOFAR, while the SKA should be able to measure the reionization history using the quadrupole moment of the power spectrum to great accuracy.

Key words: methods: numerical – dark ages, reionization, first stars.

1 INTRODUCTION

One of the periods in the history of our Universe about which we know the least is the epoch of reionization (EoR). During this epoch the first sources of light formed and gradually ionized the neutral hydrogen (H I) in the intergalactic medium (IGM). Our present understanding of this epoch is mainly constrained by observations of the cosmic microwave background (CMB) radiation (Komatsu et al. 2011; Planck Collaboration XIII 2015) and the absorption spectra of high-redshift quasars (Becker et al. 2001, 2015; Fan et al. 2003; White et al. 2003; Goto et al. 2011). These observations suggest that reionization was an extended process, spanning over the redshift range $6 \lesssim z \lesssim 15$ (see e.g. Alvarez et al. 2006; Mitra, Ferrara & Choudhury 2013; Bouwens et al. 2015; Mitra, Choudhury & Ferrara 2015; Robertson et al. 2015). Such indirect observations are, however, limited in their ability to answer several important questions regarding the EoR. These unresolved issues include the precise duration and timing of reionization, the properties of major ionizing sources, the relative contribution to the ionizing photon budget from various kinds of sources, and the typical size and distribution of ionized bubbles.

Observations of the redshifted 21 cm line, originating from spin flip transitions in neutral hydrogen atoms, are expected to be the key to resolving many of these long-standing issues. The brightness

⋆ E-mail: smaju@astro.su.se, s.majumdar@imperial.ac.uk (SM); Hannes.Jensen@physics.uu.se (HJ)

temperature of the redshifted 21 cm line directly probes the H I distribution at the epoch where the radiation originated. Observing this line enables us, in principle, to track the entire reionization history as it proceeds with redshift.

Motivated by this, a huge effort is underway to detect the redshifted 21 cm signal from the EoR using low-frequency radio interferometers, such as the GMRT (Paciga et al. 2013), LOFAR (van Haarlem et al. 2013; Yatawatta et al. 2013; Jelić et al. 2014), MWA (Bowman et al. 2013; Tingay et al. 2013), PAPER (Parsons et al. 2014) and 21CMA (Wang et al. 2013). These observations are complicated to a large degree by foreground emissions, which can be ∼4–5 orders of magnitude stronger than the expected signal (e.g. Di Matteo et al. 2002; Ali, Bharadwaj & Chengalur 2008; Jelić et al. 2008), and system noise (Morales 2005; McQuinn et al. 2006). So far only weak upper limits on the 21 cm signal have been obtained (Paciga et al. 2013; Dillon et al. 2014; Parsons et al. 2014; Ali et al. 2015).

Owing to the low sensitivity of the first generation interferometers, they will probably not be capable of directly imaging the H I distribution. This will have to wait for the arrival of the extremely sensitive next generation of telescopes such as the SKA (Mellema et al. 2013, 2015; Koopmans et al. 2015). The first-generation telescopes are instead expected to detect and characterize the signal through statistical estimators such as the variance (e.g. Patil et al. 2014) and the power spectrum (e.g. Pober et al. 2014).

Many studies to date have focused on the spherically averaged 21-cm power spectrum (e.g. McQuinn et al. 2007; Lidz et al. 2008; Barkana 2009; Iliev et al. 2012). By averaging in spherical shells in Fourier space, one can obtain good signal-to-noise for the power spectrum, while still preserving many important features of the signal. However, the spherically averaged power spectrum does not contain all information about the underlying 21 cm field. For example, as reionization progresses, the fluctuations in the H I field will make the 21 cm signal highly non-Gaussian. This non-Gaussianity cannot be captured by the power spectrum, but requires higher order statistics (Bharadwaj & Pandey 2005; Mellema et al. 2006; Watkinson & Pritchard 2014; Mondal, Bharadwaj & Majumdar 2015a).

Another important effect that cannot be captured fully by the spherically averaged power spectrum is the effect of *redshift-space distortions* caused by the peculiar velocities of matter. The coherent inflows of matter into overdense regions and the outflows of matter from underdense regions will produce an additional red- or blueshift in the 21 cm signal on top of the cosmological redshift, changing the contrast of the 21 cm signal, and making it anisotropic (Bharadwaj & Ali 2004; Barkana & Loeb 2005; McQuinn et al. 2006; Mao et al. 2012; Jensen et al. 2013; Majumdar, Bharadwaj & Choudhury 2013). The redshift-space distortions in the 21 cm signal have previously generated interest due to the possibility of extracting the purely cosmological matter power spectrum (Barkana & Loeb 2005; McQuinn et al. 2006; Shapiro et al. 2013). However, they also carry interesting astrophysical information.

It has been shown in previous studies (Jensen et al. 2013; Majumdar et al. 2013; Ghara, Choudhury & Datta 2015a) that the anisotropy in the 21 cm signal due to the redshift-space distortions will depend on the topology of reionization, or in other words on the properties of the sources of reionization. In this paper, we explore the prospects of using the 21-cm redshift-space distortions to obtain information about the sources of reionization. We calculate the evolution of the power spectrum anisotropy for a collection of simulated reionization scenarios assuming different properties of the sources of ionizing photons. We also investigate different ways of quantifying this anisotropy, and study the prospects of distinguishing between the source models in observations with current and upcoming interferometers.

The structure of this paper is as follows. In Section 2, we describe the simulations and source models that we have used to generate a collection of reionization scenarios. Here, we also describe the method that we use to include the redshift-space distortions in the simulated signal. In Section 3, we evaluate different methods of quantifying the power spectrum anisotropy and discuss the interpretation of the anisotropy using the quasi-linear model of Mao et al. (2012). In Section 4, we describe the observed large-scale features of the redshift-space anisotropy for the different reionization scenarios that we have considered. In Section 5, we discuss the feasibility of observing these anisotropic signatures in present and future radio interferometric surveys, and what we can learn from the redshift-space distortions about the reionization history. Finally, in Section 6 we summarize our findings.

Throughout the paper we present our results for the cosmological parameters from *WMAP* five-year data release: $h = 0.7$, $\Omega_{\rm m} = 0.27$, $\Omega_\Lambda = 0.73$, $\Omega_{\rm b}h^2 = 0.0226$ (Komatsu et al. 2009).

2 REIONIZATION SIMULATIONS FOR DIFFERENT SOURCE MODELS

To study the effects of the sources of reionization on the redshift-space anisotropy of the 21 cm signal, we simulate a number of different reionization scenarios, assuming different source properties. All of these simulations are based on a single *N*-body simulation of the evolving dark matter density field.

2.1 *N*-body simulations

The *N*-body simulations were carried out as part of the PRACE4LOFAR project (PRACE projects 2012061089 and 2014102339) with the CUBEP^{3}M code (Harnois-Déraps et al. 2013), which is based on the older code PMFAST (Merz, Pen & Trac 2005). Gravitational forces are calculated on a particle–particle basis at close distances, and on a mesh for longer distances. The size of our simulation volume was $500/h = 714$ Mpc (comoving) along each side. We used 6912^3 particles of mass $4.0 \times 10^7\,{\rm M}_\odot$ on a 13824^3 mesh, which was then downsampled to a 600^3 grid for modelling the reionization. Further details of the *N*-body simulation can be found in Dixon et al. (in preparation).

For each redshift output of the *N*-body simulation, haloes were identified using a spherical overdensity scheme. The minimum halo mass that we have used for our reionization simulations is $2.02 \times 10^9\,{\rm M}_\odot$.

2.2 Reionization simulations

To generate the ionization maps for our different reionization scenarios, we used a modified version of the semi-numerical code described in Choudhury, Haehnelt & Regan (2009) and Majumdar et al. (2013, 2014). This method has been tested extensively against a radiative transfer simulation and it is expected to generate the 21 cm signal from the EoR with an accuracy of ≥90 per cent (Majumdar et al. 2014) for the length scales that we will deal with in this paper.

Like most other semi-numerical methods for simulating the EoR 21 cm signal, our scheme is based on the excursion-set formalism developed by Furlanetto, Zaldarriaga & Hernquist (2004), making it similar to the methods described by Zahn et al. (2007), Mesinger & Furlanetto (2007) and Santos et al. (2010). In this method, one

compares the average number of photons in a specific volume with the average number of neutral hydrogen atoms in that volume. Here we assume that the neutral hydrogen follows the dark matter distribution.

Once we generate the dark matter density field at a fixed redshift using the *N*-body simulation, then depending on the source model of the reionization scenario under consideration (that we will discuss later in this section), we also generate an instantaneous ionizing photon field at the same redshift in a grid of the same size as that of the dark matter density field. These density fields of photons and neutral hydrogen are generally constructed in a grid coarser than the actual *N*-body resolution. In our case the resolution of this grid is 1.19 Mpc, i.e. 600^3 cells.

Next, to determine the ionization state of a grid cell, we compare the average number density of ionizing photons and neutral hydrogen atoms around it within a spherical volume. The radius of this smoothing sphere is then gradually increased, starting from the grid cell size and going up to the assumed mean free path[1] of the photons at that redshift. If, for any radius of this smoothing sphere, the average number density of photons becomes greater than or equal to the average number density of the neutral hydrogen, the cell is flagged as ionized. The same procedure is repeated for all the grid cells and an ionization field at that specific redshift is generated. A more detailed description of this simulation method can be found in Choudhury et al. (2009) and Majumdar et al. (2014).

2.2.1 Source models

Each of our simulated reionization scenarios consists of a different combination of various sources of ionizing photons. Here, we describe these different source types, and in Section 2.2.2 we describe the reionization scenarios.

(i) Ultraviolet photons from galaxies (UV): in most reionization models, galaxies residing in the collapsed dark matter haloes are assumed to be the major sources of ionizing photons. To date, much is unknown about these high-redshift galaxies and the characteristics of their radiation. Thus most simulations assume that the total number of ionizing photons contributed by a halo of mass $M_{\rm h}$ which is hosting such galaxies is simply

$$N_\gamma(M_{\rm h}) = N_{\rm ion}\frac{M_{\rm h}\Omega_{\rm b}}{m_{\rm p}\Omega_{\rm m}}. \quad (1)$$

Here, $N_{\rm ion}$ is a dimensionless constant which effectively represents the number of photons entering in the IGM per baryon in collapsed objects and $m_{\rm p}$ is the mass of a proton or hydrogen atom. Reionization simulations (whether radiative transfer or semi-numerical) which adopt this kind of model for the production of the major portions of their ionizing photons generally produce a global 'inside-out' reionization scenario (see e.g. Mellema et al. 2006; Zahn et al. 2007; Choudhury et al. 2009; Mesinger, Furlanetto & Cen 2011 etc.).

We assume that all ionizing photons generated by these kinds of sources[2] are in the ultraviolet part of the spectrum. Thus, they only affect the IGM locally, up to a distance limited by their mean free path.

(ii) Uniform ionizing background (UIB): the observed population of galaxies at high redshifts, seems unable to keep the universe ionized, unless there is a significant increase in the escape fraction of the ionizing photons from them with the increasing redshift or the galaxies below the detection thresholds of the present-day surveys contribute a significant fraction of the total ionizing photons (Kuhlen & Faucher-Giguère 2012; Mitra et al. 2013). An alternative possibility is that, if sources of hard X-ray photons (such as active galactic nuclei or X-ray binaries) were common in the early Universe, these could give rise to a more or less uniform ionizing background. Hard X-rays would easily escape their host galaxies and travel long distances before ionizing hydrogen (McQuinn 2012; Mesinger, Ferrara & Spiegel 2013).

We model this type of source as a completely uniform ionizing background that provides the same number of ionizing photons at every location. The extreme case of a 100 per cent contribution of the ionizing photons from this kind of background would lead to a global 'outside-in' reionization.

(iii) Soft X-ray photons (SXR): the escape fraction of extreme ultraviolet photons from their host galaxies is a hotly debated issue. Soft X-ray photons, on the other hand, would have little difficulty escaping from their host sources into the IGM. Also, there is a possibility that the X-ray production could have been more prevalent in the high-redshift galaxies than their low-redshift counterparts (Mirabel et al. 2011; Fragos et al. 2013).

When including this type of photons in our simulations we have considered them to be uniformly distributed around their source haloes within a radius equal to their mean free path at that redshift. To estimate the mean free path of these soft X-ray photons we have used equation 1 in McQuinn (2012) which is dependent on the redshift of their origin and the frequency of the photon. For simplicity, we assume that all the haloes that we have identified as sources will produce soft X-ray photons and all of these photons will have the same energy (200 eV). A significant contribution by these soft X-ray photons may lead to a more homogeneous reionization scenario than the case when the major portion of photons are in the ultraviolet.

(iv) Power-law mass dependent efficiency (PL): for source type (i) we have assumed that the number of UV photons generated by a galaxy is proportional to its host halo mass. Instead of this it can also be assumed that the number of photons contributed by a halo follows a power law $N_\gamma(M_{\rm h}) \propto M_{\rm h}^n$.

We consider two cases, where the power-law index is equal to 2 and 3. With this source model, higher-mass haloes produce relatively more ionizing photons, giving rise to fewer, but larger ionized regions. This model provides a crude approximation of a situation in which reionization is powered by rare bright sources, such as quasars. While the number density of quasars at high redshifts is

[1] The mean free path of ionizing photons at high redshifts is largely an unknown quantity till date. We have used a fixed maximum smoothing radius of 70 comoving Mpc at all redshifts for our fiducial reionization sources (i.e. UV sources), which is consistent with the findings of Songaila & Cowie (2010) at $z \sim 6$.

[2] Note that in our reionization scenarios we allow only haloes of mass $\geq 2.02 \times 10^9$ M$_\odot$ to host UV photon sources. In reality, faint galaxies hosted by low-mass haloes ($10^5 \leq M_{\rm h} \leq 10^9$ M$_\odot$) may produce significant amounts of UV photons during the EoR. However, there is a possibility that star formation in these low-mass haloes may also get suppressed once they have been ionized and heated to temperatures of $\sim 10^4$ K (see e.g. Couchman & Rees 1986; Gnedin 2000; Dijkstra et al. 2004; Okamoto, Gao & Theuns 2008). This poses an uncertainty in their actual role during the EoR. Further, even when one includes them in the simulations, it is very unlikely that the resulting ionization and 21 cm topology will depart from its global 'inside-out' nature, and the anisotropy of the 21-cm power spectrum – which is the focus of this paper – will not be severely sensitive to the presence of small-mass sources (we discuss this in further details in Appendix A).

Table 1. The relative contribution from different source types in our reionization scenarios. UV=ultra-violet; UIB=uniform ionizing background; SXR=soft X-ray background; PL=power-law.

Reionization	UV	UIB	SXR	PL	Non-uniform
Fiducial	100%	–	–	1.0	No
Clumping	100%	–	–	1.0	Yes
UIB dominated	20%	80%	–	1.0	No
SXR dominated	20%	–	80%	1.0	No
UV+SXR+UIB	50%	10%	40%	1.0	No
PL 2.0	–	–	–	2.0	No
PL 3.0	–	–	–	3.0	No

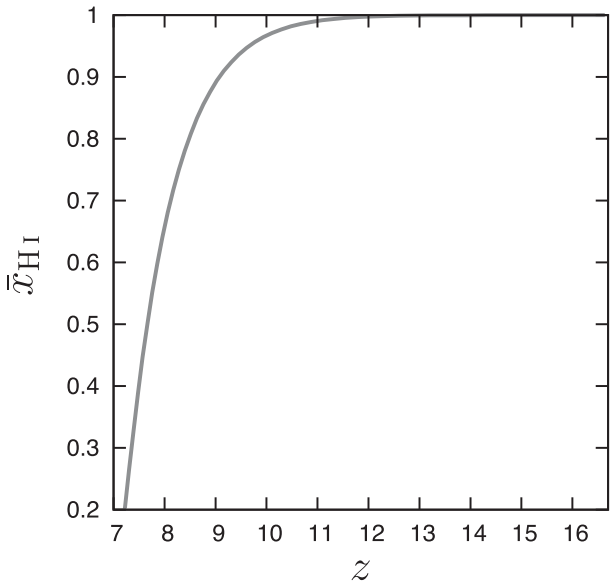

Figure 1. The evolution of the mass averaged neutral fraction with redshift for our fiducial reionization scenario. We tune all other reionization scenarios to follow the same reionization history.

not expected to be high enough to drive reionization (see e.g. Madau, Haardt & Rees 1999), this model serves as an extreme illustration of the type of topology expected from rare ionizing sources.

2.2.2 *Reionization scenarios*

The aim of this paper is to study the effect of the different source types described above on the 21-cm power spectrum anisotropy. To do this, we construct several reionization scenarios by combining the source types in different ways, as summarized in Table 1.

In our fiducial reionization scenario, 100 per cent of the ionizing photons come from galaxies residing in dark matter haloes of mass $\geq 2.02 \times 10^9\,{\rm M}_\odot$, resulting in a global inside-out reionization topology. The evolution of the reionization source population in this scenario thus follows the evolution of the collapsed fraction. Reionization starts around $z \sim 16$ (when the first ionization sources formed) and by $z = 7.221$ the mass averaged neutral fraction (designated by $\bar{x}_{\rm H\,I}$ throughout this paper) of the IGM reaches $\sim$0.2, as shown in Fig. 1. At this point, the 21 cm signal is likely too weak to detect, at least with first-generation interferometers (Jensen et al. 2013; Majumdar et al. 2013, 2014; Datta et al. 2014).

We tune $N_{\rm ion}$ at each redshift for all our reionization scenarios to follow the same evolution of $\bar{x}_{\rm H\,I}$ with z as the fiducial model (see Fig. 1). This ensures that any differences in the 21 cm signal and its anisotropy across different reionization scenarios are due solely to the source types, and not due to the underlying matter distribution. Of course this will force all scenarios except the fiducial one to follow an artificial reionization history. However, our aim here is not to produce the most realistic reionization scenarios, but rather to produce a wide range of reionization topologies and thus a significant difference in the anisotropy of the 21 cm signal.

In all of our reionization scenarios except one, we have assumed that the rate of recombination is uniform everywhere in the IGM. However, in reality, the recombination rate is expected to be dependent on the density of the ionized medium. Specifically, dense structures with sizes of the order of a few kpc, mostly unresolvable in this type of simulations, are expected to boost the recombination rate significantly and thus increase the number of ionizing photons required to complete reionization. They will also give rise to self-shielded regions like Lyman limit systems. There has been some effort in including these effects in the simulations of the large-scale EoR 21 cm signal (Choudhury et al. 2009, 2015; Sobacchi & Mesinger 2014; Shukla et al., in preparation). We have included the effects of these shelf-shielded regions in the IGM by using equation 15 in Choudhury et al. (2009). Although this approach somewhat overestimates the impact of non-uniform recombinations (due to the coarse resolution of the density fields that we use in our semi-numerical models), it can still serve to illustrate their effect on the reionization topology.

2.3 Generating redshift-space brightness temperature maps

Following the steps described in Sections 2.1 and 2.2 we have simulated coeval volumes of the matter density, ionization and velocity fields at various redshifts for the different models of reionization described in Table 1. The density and ionization fields are then combined to generate the brightness temperature maps assuming that $T_{\rm s} \gg T_{\rm CMB}$,[3] where $T_{\rm s}$ and $T_{\rm CMB}$ are the spin temperature and the CMB temperatures, respectively. We then take into account the peculiar velocities in order to construct the redshift-space signal. By redshift space, we mean the space that will be reconstructed by an observer assuming that all redshifts are purely due to the Hubble expansion. An emitter with a line-of-sight peculiar velocity $v_\parallel$ at a real-space position $\boldsymbol{r}$ will be translated to an apparent redshift-space position $\boldsymbol{s}$ following

$$\boldsymbol{s} = \boldsymbol{r} + \frac{1+z}{H(z)} v_\parallel \hat{\boldsymbol{r}}. \quad (2)$$

For a more in-depth explanation of 21-cm redshift-space distortions, see e.g. Mao et al. (2012), Jensen et al. (2013) or Majumdar et al. (2013).

We implement the redshift-space distortions using the same method as in Jensen et al. (2013). This method splits each cell into n smaller sub-cells along the line of sight and assigns each sub-cell the brightness temperature $\delta T_{\rm b}(\boldsymbol{r})/n$, where $\delta T_{\rm b}(\boldsymbol{r})$ is the temperature of the host cell. It then moves the sub-cells according to equation (2), and regrids them to the original

[3] Note that we have not taken into account the effect of fluctuations in the spin temperature. Spin temperature fluctuations due to Lyman α pumping and heating by X-ray sources can affect the 21-cm brightness temperature fluctuations significantly during the early stages of the EoR (Mao et al. 2012; Mesinger et al. 2013; Ghara et al. 2015a). However, as we discuss in the later parts of this paper (Section 4.1), the anisotropy in the 21-cm power spectrum will not be strongly affected by this, especially once the early phase of EoR is over (i.e. when $\bar{x}_{\rm H\,I} \leq 0.95$).

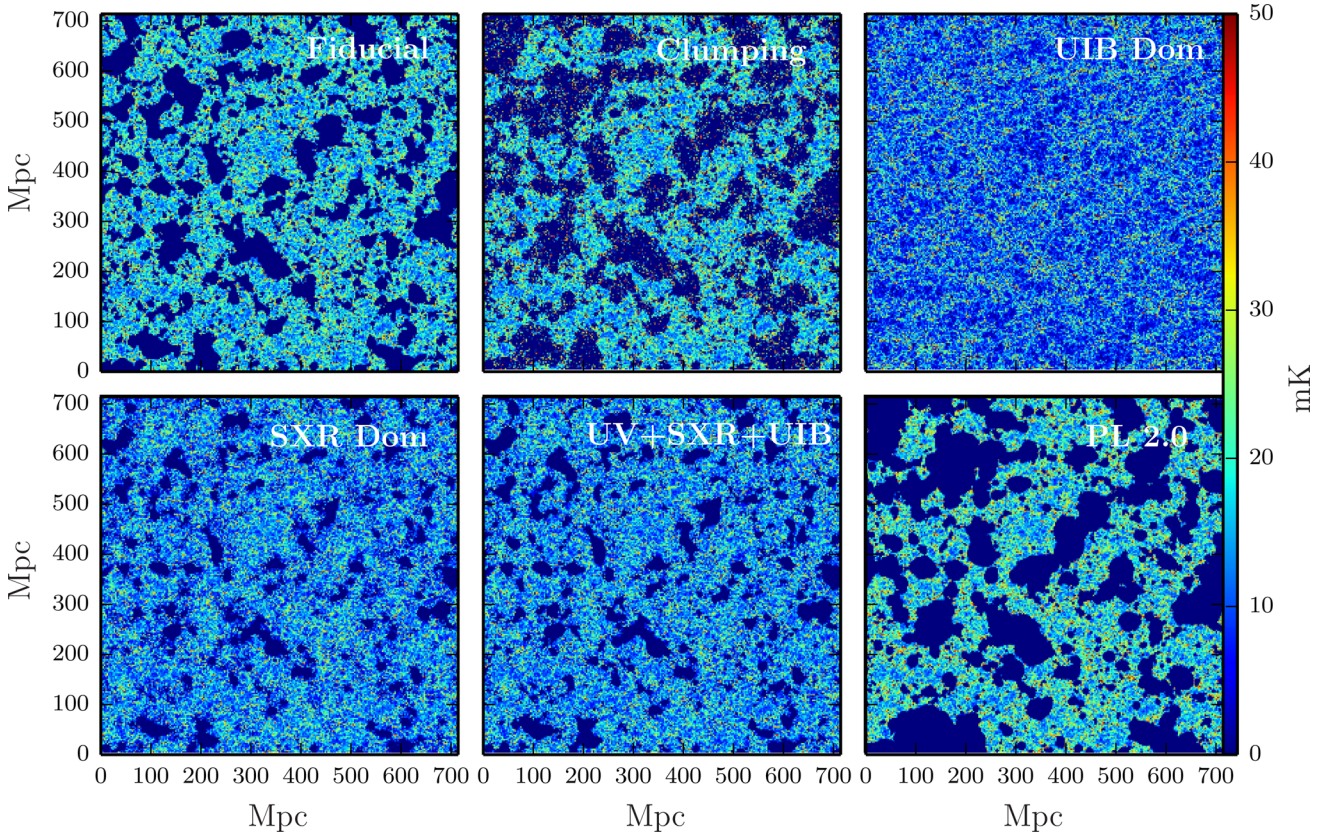

Figure 2. Redshift-space brightness temperature maps for six of our reionization scenarios. The line of sight is along the y-axis. The mass averaged neutral fraction for all the panels is $\bar{x}_{\rm Hi} = 0.5$.

resolution. Here, we use $n = 50$, which gives results that are accurate down to approximately one-fourth of the Nyquist wavenumber, or $k \lesssim k_{\rm N}/4 = \pi/4 \times 600/(714\ {\rm Mpc}) = 0.66\ {\rm Mpc}^{-1}$ (Mao et al. 2012; Jensen et al. 2013). Fig. 2 shows the resulting redshift-space brightness temperature maps for six of the seven different reionization scenarios considered here (at a time when the reionization had reached 50 per cent).

3 QUANTIFYING THE POWER SPECTRUM ANISOTROPY

Since only the line-of-sight component of the peculiar velocities affects the 21 cm signal, redshift-space distortions will make the observed 21-cm power spectrum anisotropic. To quantify this anisotropy, it is common to introduce a parameter μ, defined as the cosine of the angle between a wavenumber $\boldsymbol{k}$ and the line of sight. The redshift-space power spectrum of the EoR 21 cm signal at large scales can be written as a fourth-order polynomial in μ under the quasi-linear approximation for the signal presented by Mao et al. (2012). This quasi-linear model is an improvement on the linear model of Bharadwaj & Ali (2005) and Barkana & Loeb (2005) for the 21 cm signal. In the quasi-linear model one assumes the density and velocity fluctuations to be linear in nature but the fluctuations in the neutral fraction are considered to be non-linear. The expression for the 21-cm power spectrum, $P^{\rm s}(k, \mu)$, becomes

$$P^{\rm s}(k,\mu) = \overline{\delta T_{\rm b}}^2(z)\left[P_{\rho_{\rm Hi},\rho_{\rm Hi}}(k) + \right. \\ \left. +2\mu^2 P_{\rho_{\rm Hi},\rho_{\rm M}}(k) + \mu^4 P_{\rho_{\rm M},\rho_{\rm M}}(k)\right], \quad (3)$$

where $\rho_{\rm Hi}$ is the neutral hydrogen density, and $\rho_{\rm M}$ is the total hydrogen density.

It has been suggested that this form of decomposition can be used to extract the cosmology from the astrophysics on large spatial scales, by extracting the coefficient of the μ^4-term in equation (3) (Barkana & Loeb 2005; McQuinn et al. 2006; Shapiro et al. 2013). However, this is very challenging due to the high level of cosmic variance at these length scales and also due to the fact that this decomposition is in a non-orthonormal basis.

However, the astrophysical information contained in the μ^2 term is also interesting. This term is determined by the cross-power spectrum of the neutral matter density and the total matter density, which is a measure of the 'inside-outness' of the reionization topology (Jensen et al. 2013; Majumdar et al. 2013; Ghara et al. 2015a). However, extracting this term from noisy data using equation (3) is also challenging since power tends to leak over between the μ^2 and μ^4 terms (Jensen et al. 2013).

One way to deal with this is to measure the sum of the μ^2 and μ^4 terms (Jensen et al. 2013). This quantity is much more resistant to noise. It will contain a mixture of cosmological and astrophysical information but since the cosmological matter power spectrum evolves only slowly and monotonically, the *evolution* of the sum of the μ terms will be mostly determined by the μ^2 term.

A different approach is to instead expand the power spectrum in the orthonormal basis of Legendre polynomials – a well-known approach in the field of galaxy redshift surveys (Hamilton 1992, 1998; Cole, Fisher & Weinberg 1995). In this representation, the power spectrum can be expressed as a sum of the even multipoles

of Legendre polynomials:

$$P^{\rm s}(k,\mu) = \sum_{l\ \rm even} \mathcal{P}(\mu) P_{\rm l}^{\rm s}(k). \quad (4)$$

From an observed or simulated 21-cm power spectrum, one can calculate the angular multipoles $P_{\rm l}^{\rm s}$:

$$P_{\rm l}^{\rm s}(k) = \frac{2l+1}{4\pi} \int \mathcal{P}(\mu) P^{\rm s}(k) {\rm d}\Omega. \quad (5)$$

The integral is done over the entire solid angle to take into account all possible orientations of the $\boldsymbol{k}$ vector with the line-of-sight direction. The estimation of each multipole moment through equation (5) will be independent of the other, as this representation is in an orthonormal basis.

Under the quasi-linear model of Mao et al. (2012), only the first three even multipole moments will have non-zero values (Majumdar et al. 2013, 2014):

$$P_0^{\rm s} = \overline{\delta T_{\rm b}}^2 \left[\frac{1}{5} P_{\rho_{\rm M},\rho_{\rm M}} + P_{\rho_{\rm Hi},\rho_{\rm Hi}} + \frac{2}{3} P_{\rho_{\rm Hi},\rho_{\rm M}} \right] \quad (6)$$

$$P_2^{\rm s} = 4\overline{\delta T_{\rm b}}^2 \left[\frac{1}{7} P_{\rho_{\rm M},\rho_{\rm M}} + \frac{1}{3} P_{\rho_{\rm Hi},\rho_{\rm M}} \right] \quad (7)$$

$$P_4^{\rm s} = \frac{8}{35} \overline{\delta T_{\rm b}}^2 P_{\rho_{\rm M},\rho_{\rm M}}. \quad (8)$$

The monopole moment $P_0^{\rm s}$ is, by definition (equation 5), the spherically averaged power spectrum. We see that the quadrupole moment, $P_2^{\rm s}$, is a linear combination of $P_{\rho_{\rm M},\rho_{\rm M}}$ and $P_{\rho_{\rm Hi},\rho_{\rm M}}$, just as the sum of the μ^2 and μ^4 terms in equation (3). Both the sum of the μ^2 and μ^4 terms in equation (3) and $P_2^{\rm s}$ in equation (7) thus contain the same physical information. However, in contrast to the decomposition of the power spectrum in terms of powers of μ, the expansion in the Legendre polynomials is in an orthonormal basis, which means that the uncertainty in the estimates of one moment will be uncorrelated with the uncertainty in the estimates of the other moments. Therefore, the multipole moments should be easier to extract from noisy data. This also implies that, if measured with statistical significance, each multipole moment can be used as an independent and complementary estimator of the cosmological 21 cm signal.

To test this, we took simulated brightness temperature volumes from the fiducial model (see Section 2.2) and added 50 different realizations of Gaussian noise (later on, we will make predictions with realistic noise for LOFAR and the SKA). After calculating the power spectra of the noisy data volumes, we fit a fourth-order polynomial in μ using standard least-squares fitting, and also estimated the $P_2^{\rm s}$ moment using equation (5). The results of this test are shown in Fig. 3. The top panel shows the measured values of the anisotropy using the two methods. The solid lines show the true noise-free values, and the error bars show the 2σ variation in the noisy measurements across the different noise realizations. In the bottom panel, we show a histogram of the ratio between the measured and the true value for two methods. While the difference is not dramatic, we see here that the $P_2^{\rm s}$ is slightly more resistant to noise than the sum of the μ terms. Because of this and also due to the fact that each multipole moment represented in the orthonormal basis of Legendre polynomials will be independent of the other, we will use the quadrupole moment $P_2^{\rm s}$, as our measure of power spectrum anisotropy for the rest of this paper.

Fluctuations in spin temperature $T_{\rm s}$, introduced due to the heating by the very early astrophysical sources will affect the monopole moment ($P_0^{\rm s}$) or the spherically averaged power spectrum significantly (Fialkov, Barkana & Visbal 2014; Ghara et al. 2015a). However we expect that they will not have much impact on the anisotropy term or the quadrupole moment ($P_2^{\rm s}$). We direct the reader to Section 4.1 for further details.

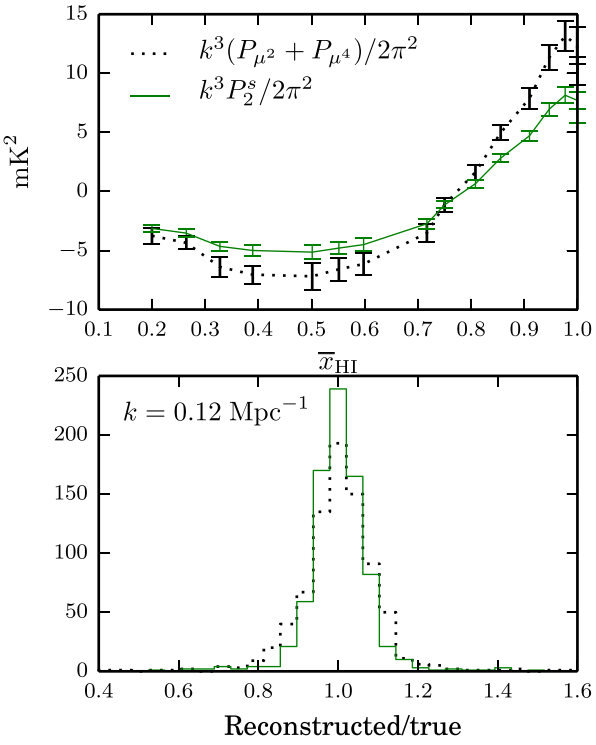

Figure 3. Comparison of the two different ways of measuring the anisotropy. The top panel shows the anisotropy reconstructed from noisy data (see the text for details) as a function of neutral fraction. The error bars show the 2σ variation for 50 different noise realizations. The bottom panel shows a histogram of the reconstructed noisy values divided by the true values. A narrower distribution around 1 is an indication of a better reconstruction.

3.1 How good is the quasi-linear model for interpreting the anisotropy?

The quadrupole moment gives us a measure of the power spectrum anisotropy. Ideally, we would want to connect this measure to the topology of reionization. The quasi-linear approximation gives us a way to do this in the early stages of reionization and for large length scales. When this approximation holds, equation (7) tells us that $P_2^{\rm s}$ is a weighted sum of the matter power spectrum and the cross-power spectrum of the total and neutral matter densities. This cross-power spectrum measures how strongly correlated the H I and matter distributions are. If reionization is strongly inside-out, this quantity will decrease quickly as reionization progresses, and take on a negative value (see e.g. Jensen et al. 2013; Majumdar et al. 2013; Ghara et al. 2015a).

To some degree, the success of the quasi-linear approximation depends on the source model. In Fig. 4, we show the ratio between the true value of $P_2^{\rm s}$ and the quasi-linear expectation, constructed by first calculating $P_{\rho_{\rm M},\rho_{\rm M}}$ and $P_{\rho_{\rm Hi},\rho_{\rm M}}$ and then combining them according to equation (7). We see that at $k = 0.12$ Mpc^{-1}, the approximation works rather well (i.e. the ratio is close to 1) for all scenarios up to around $\bar{x}_{\rm Hi} \sim 0.5$. For larger spatial scales, the effect

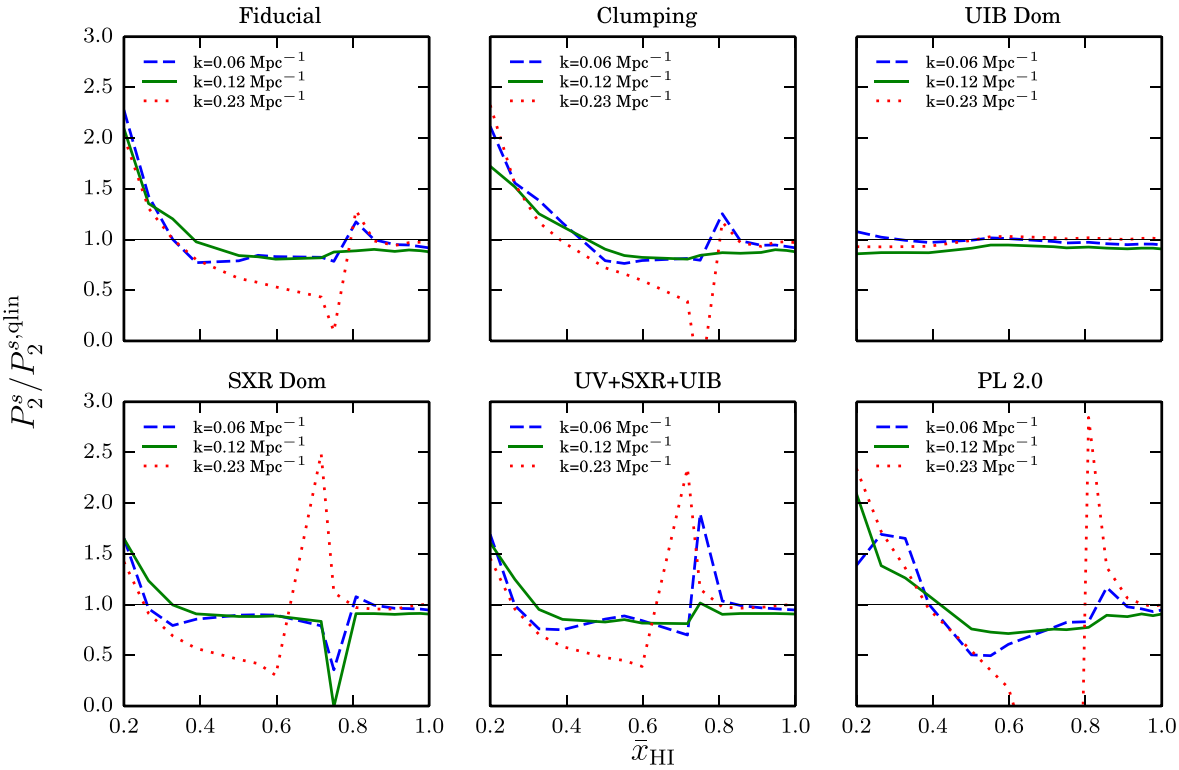

Figure 4. The ratio between the quadrupole moment measured from the simulated 21 cm signal, and the quasi-linear approximation, calculated from equation (7) for our different reionization scenarios.

of sample variance becomes significant, while at smaller spatial scales, non-linearities start influencing the results. The quasi-linear approximation for the signal works poorly for the PL 2.0 scenario, but works almost perfectly until very late stages of EoR for the UIB dominated scenario. Around $\bar{x}_{\mathrm{Hi}} = 0.7$, the quadrupole moment crosses zero, giving rise to sudden jumps in the ratio.

Note that the quadrupole moment of the power spectrum is a quantity that can always be calculated from the data, even when the signal is highly non-linear and also regardless of the assumed model for the signal. The quasi-linear model is simply a tool to help with interpreting the quantity. The quadrupole moment will still be useful as an independent estimator of the signal and as an observable to distinguish between different source models even in the non-linear regime. Here, all we can do is look at how this estimator evolves in simulations with different reionization scenarios, which we discuss in the next section.

4 REDSHIFT-SPACE DISTORTIONS IN DIFFERENT REIONIZATION SCENARIOS

In Fig. 5, we show the monopole moment of the power spectrum P_0^s – which is by definition the spherically averaged power spectrum – for the reionization scenarios listed in Table 1. From here onwards we show all our results for the wavenumber $k = 0.12\mathrm{Mpc}^{-1}$. It is expected that LOFAR will be most sensitive around this length scale (Jensen et al. 2013) and also the quasi-linear approximations seems to work quite well for this length scale (Fig. 4). The quantity P_0^s has been studied extensively before (e.g. Santos et al. 2010; Mesinger et al. 2011; Mao et al. 2012; Jensen et al. 2013; Majumdar et al. 2013; Ghara et al. 2015a etc.), and the trends we are observing here mostly agree with these previous studies.

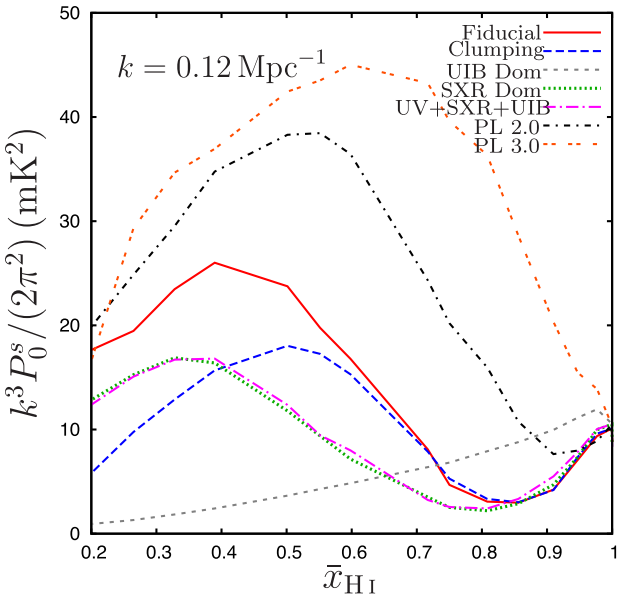

Figure 5. The monopole moment of the power spectrum for all of our reionization scenarios as a function of the global neutral fraction at $k = 0.12$ Mpc^{-1}.

At the large scales we consider here, the behaviour of P_0^s can be readily understood by the quasi-linear approximation (equation 6). Initially, the brightness temperature fluctuations mostly come from fluctuations in the H I distribution, and P_0^s decreases as the density peaks are ionized. Later on, at a neutral fraction around 0.3–0.5 (depending on the reionization scenario), a peak in P_0^s appears, as large ionized regions form and become the main contributors to the

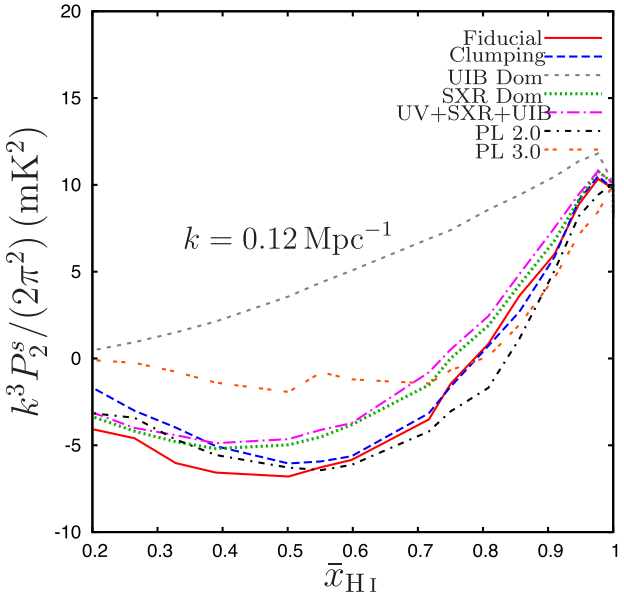

Figure 6. The quadrupole moment of the power spectrum for all of our reionization scenarios as a function of the global neutral fraction at $k = 0.12\,\mathrm{Mpc}^{-1}$.

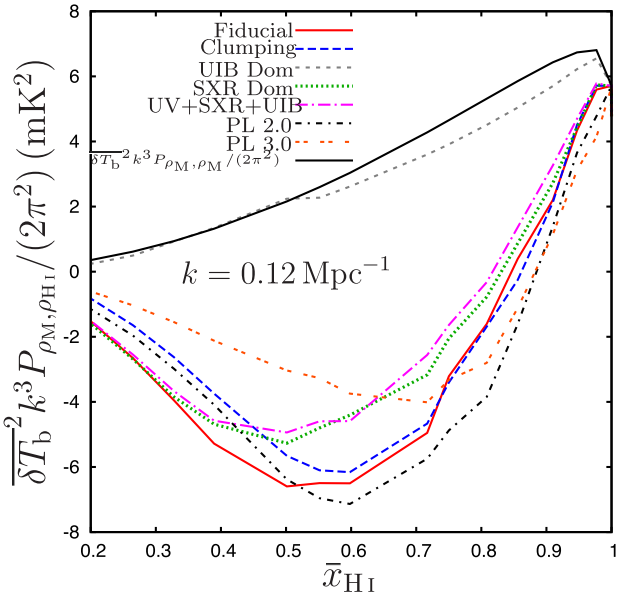

Figure 7. The matter and H I density cross-power spectrum as a function of the global neutral fraction for all the reionization scenarios at $k = 0.12\,\mathrm{Mpc}^{-1}$. The black solid line shows the evolution of the matter power spectrum with $\bar{x}_{\mathrm{H\,I}}$, which is same for all the reionization scenarios considered here.

brightness temperature fluctuations. This peak is especially pronounced in the PL scenarios, where the ionized bubbles are particularly large. However, it is completely absent in the UIB dominated scenario, since due to the presence of a uniform ionizing background the H I distribution at all stages follows the product of the matter distribution and the mean brightness temperature, which causes P_0^s to fall off monotonically with decreasing $\bar{x}_{\mathrm{H\,I}}$.

Fig. 6 shows the quadrupole moment, P_2^s, which we use as a measure of the power spectrum anisotropy. It was also studied in Majumdar et al. (2013) and Majumdar et al. (2014) for EoR scenarios similar to the fiducial and clumping scenarios described in this paper. As we saw previously (Section 3.1), the behaviour of P_2^s can be understood to some degree using the quasi-linear model (equation 7), where P_2^s is a linear combination of the matter power spectrum $P_{\rho_\mathrm{M},\rho_\mathrm{M}}$ and the cross-power spectrum between the total matter density and the neutral matter density, $P_{\rho_{\mathrm{H\,I}},\rho_\mathrm{M}}$. We show the product of the square of the mean brightness temperature ($\overline{\delta T_\mathrm{b}}^2$) and the cross-power spectrum for the different reionization scenarios in Fig. 7, along with the product of the $\overline{\delta T_\mathrm{b}}^2$ and the matter power spectrum (which is the same for all the scenarios). Since the matter power spectrum increases slowly and monotonously and $\overline{\delta T_\mathrm{b}}^2$ decreases rather rapidly with the decreasing $\bar{x}_{\mathrm{H\,I}}$, the evolution of the term $\overline{\delta T_\mathrm{b}}^2 P_{\rho_\mathrm{M},\rho_\mathrm{M}}$ is driven by the evolution of $\overline{\delta T_\mathrm{b}}^2$. As the contribution from the term $\overline{\delta T_\mathrm{b}}^2 P_{\rho_\mathrm{M},\rho_\mathrm{M}}$ is the same for all the reionization scenarios considered here, the major differences between P_2^s for different reionization scenarios come from the differences in the evolution of $\overline{\delta T_\mathrm{b}}^2 P_{\rho_\mathrm{M},\rho_{\mathrm{H\,I}}}$. Going back to Fig. 6, for most scenarios P_2^s initially increases in strength and then starts falling. This is because when the IGM is completely neutral, $\rho_{\mathrm{H\,I}} = \rho_\mathrm{M}$ and $P_{\rho_{\mathrm{H\,I}},\rho_\mathrm{M}}$ will increase when the matter fluctuations grow. As the most massive peaks are ionized, however, $\rho_{\mathrm{H\,I}}$ becomes anticorrelated with ρ_M and P_2^s becomes negative. The stronger the anticorrelation – i.e. the more inside-out the reionization topology is – the more negative P_2^s becomes. The scenarios that stand out from the rest are again the UIB dominated scenario, where the reionization is more outside-in than inside-out, and the PL 3 scenario. In the latter, reionization

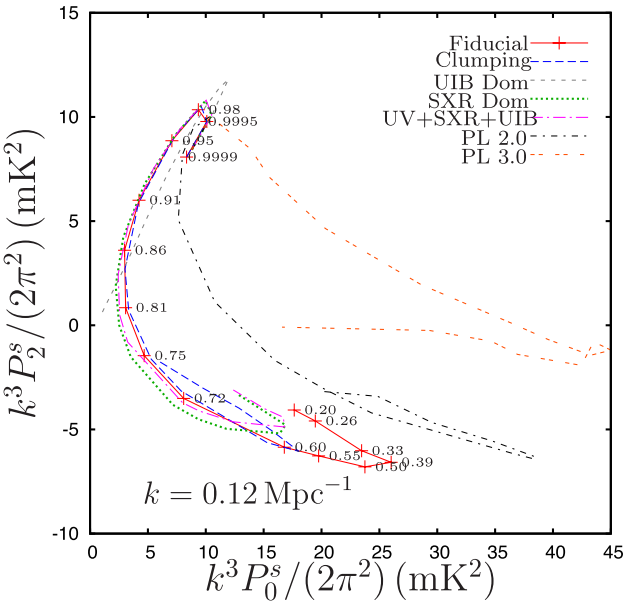

Figure 8. Trajectories of the different reionization scenarios in $P_2^s - P_0^s$ phase space for $k = 0.12\,\mathrm{Mpc}^{-1}$. The corresponding values of $\bar{x}_{\mathrm{H\,I}}$ have been printed on the trajectory of the fiducial scenario showing the global neutral fraction. For clarity, this has been shown only for the fiducial scenario.

is driven mainly by a few massive sources that produce very large regions of ionized hydrogen (H II). Since these H II bubbles are so large, the correlation between the total matter and H I field becomes very weak at large scales, and so P_2^s remains close to zero for most of the reionization history.

Since P_0^s and P_2^s are two independent but complementary measurements of the 21 cm signal, one can thus visualize the evolution of the 21 cm signal in a reionization scenario as a trajectory in the phase space of P_0^s and P_2^s. In Fig. 8 we show the reionization

scenarios considered here in such a phase-space diagram. Looking first at the fiducial scenario, it initially moves upwards to the right, with both P_0^s and P_2^s increasing as the matter fluctuations grow. At an ionization fraction of a few per cent, it starts moving downwards in an arc, eventually reaching another turnaround point at $\bar{x}_{\rm H\,I} \sim 0.4$. The point where the H I fluctuations are at their strongest seems to roughly coincide with the point where P_2^s reaches its minimum. After this, the trajectory approaches the (0, 0) point of the phase space, as the IGM becomes more and more ionized and the 21 cm signal starts to disappear.

From Figs 8 and 6, we see that the power spectrum anisotropy (i.e. P_2^s) evolves remarkably similarly in most of the reionization scenarios, even when the spherically averaged power spectrum (i.e. P_0^s) differs. The slope is very similar in the early stages of reionization, and the minima in P_2^s occur at around $\bar{x}_{\rm H\,I} \sim 0.5$ for all reionization scenarios except the extreme UIB dominated scenario.

In Appendix A we show that the strongest contributing factor to the evolution of P_2^s is the phase difference between the matter and the H I fields. As long as a major portion of the ionizing flux originates from the high-density regions (or the collapsed objects), the phase difference between the two fields will evolve in roughly the same way regardless of the strength of the H I fluctuations. Only in extreme scenarios such as our UIB dominated scenario – where the flux is evenly distributed – does the phase difference deviate from the other scenarios.

Thus, the power spectrum anisotropy will probably not be useful in telling different source models apart, unless the sources are extreme in some sense. However, it appears to offer a robust way of measuring the history of reionization. We discuss this in more detail in the next section.

4.1 The effects of spin temperature fluctuations

In the reionization scenarios discussed here we have not considered the effect of spin temperature fluctuations due to Lyman α pumping and heating by X-ray sources. These effects can influence the 21-cm brightness temperature fluctuations significantly during the early stages of EoR, if the heating of the IGM is late (Fialkov et al. 2014). This can also affect the line-of-sight anisotropy in the signal (Fialkov, Barkana & Cohen 2015, Ghara, Datta & Choudhury 2015b; Ghara et al. 2015a). In a late-heating scenario, if we define the spin temperature fluctuations in the H I distribution as

$$\eta(z, \boldsymbol{x}) = 1 - \frac{T_{\rm CMB}(z)}{T_{\rm S}(z, \boldsymbol{x})}, \tag{9}$$

then the angular multipole moments of the redshift-space power spectrum under the quasi-linear approximations will take the form

$$P_0^s = \overline{\delta T_{\rm b}}^2(z) \left[\frac{1}{5} P_{\rho_{\rm M},\rho_{\rm M}} + P_{\rho_{\rm H\,I},\rho_{\rm H\,I}} + P_{\eta,\eta} + \right. \\ \left. + 2P_{\eta,\rho_{\rm H\,I}} + \frac{2}{3} P_{\rho_{\rm H\,I},\rho_{\rm M}} + \frac{2}{3} P_{\eta,\rho_{\rm M}} \right] \tag{10}$$

$$P_2^s = 4\,\overline{\delta T_{\rm b}}^2(z) \left[\frac{1}{7} P_{\rho_{\rm M},\rho_{\rm M}} + \frac{1}{3} P_{\rho_{\rm H\,I},\rho_{\rm M}} + \frac{1}{3} P_{\eta,\rho_{\rm M}} \right] \tag{11}$$

$$P_4^s = \frac{8}{35}\,\overline{\delta T_{\rm b}}^2(z)\, P_{\rho_{\rm M},\rho_{\rm M}}. \tag{12}$$

As shown by Fialkov et al. (2014), Ghara et al. (2015a) and Ghara et al. (2015b), the spin temperature fluctuations affect the monopole moment of the power spectrum (i.e. the spherically averaged power spectrum) most severely. Figs 8 and 9 in Ghara et al. (2015a) show that the amplitude of the power spectrum gets amplified significantly at all length scales (by at least two orders of magnitude) during the cosmic dawn (when the first X-ray sources emerge) and there is a prominent dip in its amplitude at large length scales during the early phases of reionization (i.e. when $\bar{x}_{\rm H\,I} \approx 0.95$). This behaviour of the spherically averaged power spectrum is due to the fact that during the cosmic dawn and the early stages of the EoR, the auto power spectrum of the spin temperature fluctuations, $P_{\eta,\eta}$, makes the dominant contribution to the monopole moment (see fig. 10 of Ghara et al. 2015a). This term will be zero when one assumes that $T_{\rm s} \gg T_{\rm CMB}$. They have not estimated any higher order multipole moments of the power spectrum from their simulations.

However, as we can see from equation (11), the $P_{\eta,\eta}$ term does not contribute to the quadrupole moment which we use in this paper to quantify the redshift-space anisotropy in the power spectrum. The only contribution from spin temperature fluctuations to P_2^s is the cross-power spectrum of the spin temperature fluctuations and the matter density fluctuations, $P_{\eta,\rho_{\rm M}}$. In the case of late heating, Ghara et al. (2015a) find that the $P_{\eta,\rho_{\rm M}}$ term is comparable to $P_{\rho_{\rm H\,I},\rho_{\rm M}}$ at large scales during the very early stages of the EoR (i.e. $\bar{x}_{\rm H\,I} \sim 1.0-0.95$), but later on, it becomes few orders of magnitude smaller. The evolution of $P_{\eta,\rho_{\rm M}}$ with redshift and $\bar{x}_{\rm H\,I}$ as shown in Ghara et al. (2015a), may vary depending on the properties of the heating sources. These results thus suggest that the quadrupole moment is not completely immune to spin temperature fluctuations, but it is much less sensitive than the monopole moment.

5 OBSERVABILITY OF THE REDSHIFT-SPACE ANISOTROPY

Having seen how the power spectrum anisotropy behaves under idealized conditions, we now explore some of the complications one will encounter when attempting to observe this effect.

5.1 The light-cone effect

In the previous section, we showed the 21-cm power spectra estimated from so-called 'coeval' data volumes, i.e. the direct outputs from simulations, where the signal is at a fixed evolutionary stage in the entire volume. Because of the finite travel time of light, an observer will not be able to observe the signal like this. Instead, the signal will be seen at a different evolutionary stage at each observed frequency. This is known as the light-cone effect.

Because of the light-cone effect, a three-dimensional measurement of the 21 cm signal can never be done at a fixed single neutral fraction. To measure, say, the power spectrum from a real observation, one has to average over some frequency range (corresponding to a range in neutral fraction). This averaging has been shown to have a small effect on the spherically averaged power spectrum (Datta et al. 2012).[4] It has also been shown that the light-cone effect does not by itself introduce any significant additional anisotropy in the 21 cm signal at measurable scales (Datta et al. 2014). However, the averaging will have some effect on the measurements of the anisotropy that is already present due to the redshift-space distortions.

[4] The light-cone averaging could have a significant impact on the spherically averaged power spectrum, especially during the early stages of EoR, if one considers the spin temperature fluctuations in the signal due to the inhomogeneous heating by the X-ray sources and considers averaging the signal for a significantly large frequency bandwidth (Ghara et al. 2015b).

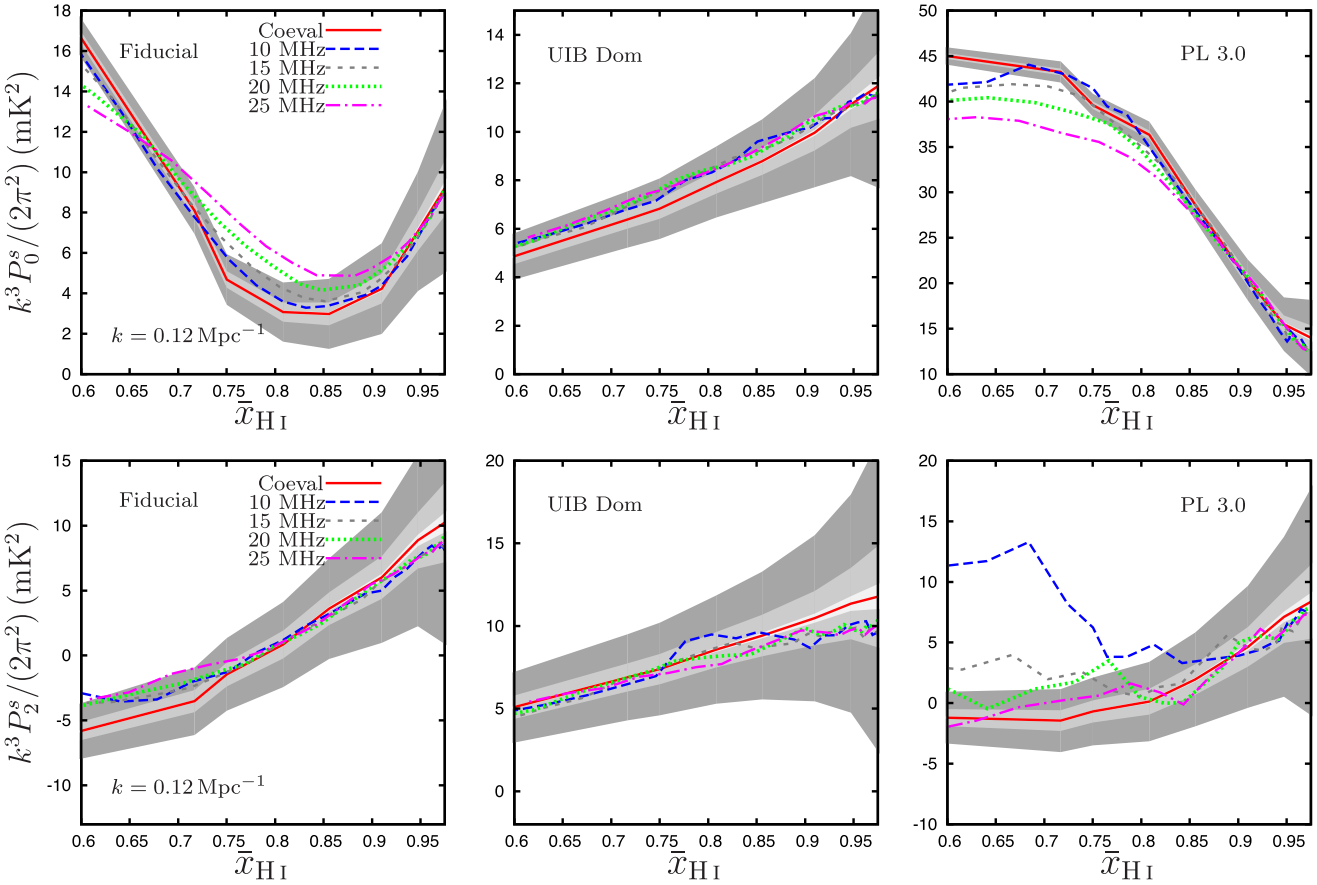

Figure 9. The monopole and quadrupole moments of the power spectrum for three different reionization scenarios as a function of global neutral fraction at $k = 0.12$ Mpc^{-1} estimated from the light-cone cubes with different frequency bandwidths. Note that for the light-cone cube results the $\bar{x}_{\mathrm{H\,I}}$ values quoted in the x-axis of these plots are the effective $\bar{x}_{\mathrm{H\,I}}$ values within the sub-volume limited by the bandwidth. The shaded regions in three different shades of grey, dark to light, show the 1σ uncertainty in these estimates due to the system noise, measured in a bandwidth of 20 MHz, after 1000 and 3000 h of LOFAR and 100 h SKA observations, respectively.

In Fig. 9, we show the monopole and the quadrupole moments of the power spectrum estimated from light-cone volumes generated as described in Section 2.3. We compare the results for coeval data volumes with bandwidths of 10, 15, 20 and 25 MHz for the fiducial reionization scenario, along with the two most extreme scenarios: the UIB dominated and PL 3 scenarios. In general, a narrower bandwidth means that the effective averaging is done over a smaller range of neutral fractions, and the value of P_2^s and P_0^s will follow the coeval values more closely. However, a narrow bandwidth will increase the sample variance.

Fig. 9 shows that for the fiducial scenario, the light-cone effect changes P_2^s only marginally, and only at low neutral fractions. The effect is strongest for the other two scenarios, but this is mostly due to sample variance, as the signal is being measured over a narrow slice of the full volume. The light-cone effect on P_0^s is largest around $\bar{x}_{\mathrm{H\,I}} \sim 0.8$ for the fiducial model. For the other two reionization scenarios it is more prominent at low neutral fractions.

5.2 Detector noise

Any radio interferometric measurement of the 21 cm signal from the EoR will face several obstacles, including detector noise, galactic and extragalactic foreground sources and ionospheric disturbances. While a full treatment of all these effects is beyond the scope of this paper, we do investigate the fundamental limitations from detector noise and foregrounds for LOFAR and the SKA.

To calculate the detector noise, we use the same method as in Jensen et al. (2013). We begin by calculating the u, v coverage for the antenna distribution in the LOFAR core (Yatawatta et al. 2013). For the SKA, we assume a Gaussian distribution of antennas within a radius of around 2000 m (Dewdney et al. 2013), assuming 150 antenna stations.

We fill the u, v planes with randomly generated Gaussian noise with a magnitude calculated using the formalism from McQuinn et al. (2006). We use the same parameters for LOFAR as in Jensen et al. (2013). For the SKA we assume a total collecting area of 5×10^5 m^2. This collecting area, along with the assumptions for the baseline distribution, is consistent with the current plans for the first-phase version of the low-frequency part of the SKA (SKA1-LOW; Koopmans et al. 2015).

Finally, we Fourier transform the noise in the u, v plane to get the noise in the image plane. We do this for many different frequencies to get a noise light-cone with the same dimensions as our signal light-cones. Here, we do not take into account the frequency dependence of the u, v coverage.

Using these simulated noise light-cones, we can then calculate the power spectrum error due to detector noise. In Fig. 9, we show these errors for 1000 and 3000 h of LOFAR observations and 100 h of SKA observations as shaded regions (in three different shades

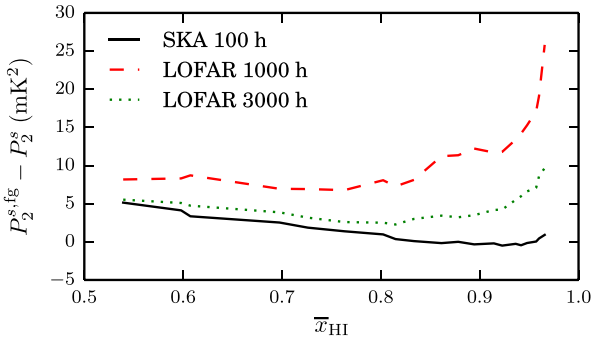

Figure 10. Effects of foreground subtraction on P_2^s. The figure shows the difference between P_2^s measured after and before adding and subtracting foreground for a few different integration times for LOFAR and the SKA. The results are shown at $k = 0.12$ Mpc^{-1} for the fiducial scenario, with the measurements carried out at 15 MHz bandwidth.

of grey, dark to light, respectively). We see that for LOFAR, the noise error for P_2^s is much higher than the uncertainty due to the light-cone effect. Clearly, LOFAR will require a long integration time to measure the evolution in P_2^s. For the SKA, however, the noise error is almost negligible, even for relatively short integration times. In this case, the light-cone effect also becomes important, at least at the later stages of reionization.

5.3 Foregrounds and PSF effects

In addition to detector noise, there are many other issues that will complicate the extraction of P_2^s from a real measurement. One major obstacle is foreground emission from Galactic and extra-Galactic sources. To properly measure the power spectrum anisotropy, the foregrounds need to be removed from the data using some algorithm.

We simulate foreground emission from diffuse and localized Galactic synchrotron radiation, Galactic free–free radiation and extragalactic bright radio sources using the methods described in Jelić et al. (2008, 2010). After adding these sources to the simulated signal, we use the GMCA algorithm to model and remove them (see Chapman et al. 2013 for a detailed description). GMCA (Generalized Morphological Component Analysis) works by attempting to express the full signal+foregrounds in a wavelet basis where only a few components are non-zero. Since the signal is very weak compared to the foregrounds, it will tend not to be included in the wavelet basis and can thus be separated from the foregrounds.

A second complication is the beam, or the point-spread function (PSF), of the instrument. The effect of the PSF is essentially a smoothing in the sky plane, de-emphasizing large $k_\perp$ modes and introducing an anisotropy in the signal. To properly study the feasibility of extracting P_2^s from real measurements, we would need to model the frequency-dependent PSF and compensate for its effects, which is beyond the scope of this paper. Instead, we simply calculate the change in $P_2^s(\bar{x}_{Hi})$ after adding and subtracting foregrounds. This change is shown in Fig. 10 for a few different integration times. Here, $P_2^{s,fg}$ denotes the quadrupole moment after adding and subtracting foregrounds, while P_2^s is the quadrupole with no foreground effects included. We show only the absolute error since the relative error fluctuates wildly where the signal crosses zero.

We see that for low noise levels, the foregrounds change the measured P_2^s by a few mK^2. As seen in Fig. 6, the signal itself ranges between approximately -5 and 10 mK^2. For the SKA, the foreground removal is almost perfect at high values of $\bar{x}_{Hi}$, while LOFAR observations appear to require long integration times to properly measure P_2^s. However, the GMCA algorithm used here is not the only method for removing foregrounds, and it remains possible that other algorithms perform better for this particular task.

5.4 Reconstructing the reionization history

As we saw in Fig. 6, the quadrupole moment evolves very predictably as a function of $\bar{x}_{Hi}$; much more so than the monopole moment or the spherically averaged power spectrum (Fig. 5). The only scenarios that deviate from the rest are the UIB dominated scenario and – for low neutral fractions – the PL 3.0 scenario. A real-life measurement would give P_2^s as a function of z, so if we assume that $P_2^s(\bar{x}_{Hi})$ is known, we can use this to reconstruct the reionization history, i.e. $\bar{x}_{Hi}(z)$. Here, we attempt to do this for our mock observations.

We begin by parametrizing $\bar{x}_{Hi}(z)$ as follows:

$$\bar{x}_{Hi}(z) = \begin{cases} 0 & \text{if} z < z_r \\ 1 - \exp[-\beta(z - z_r)] & \text{if} z \geq z_r. \end{cases} \quad (13)$$

The parameters z_r and β give the endpoint and extent of reionization, respectively (higher values of β indicate a more rapid reionization). Given values of z_r and β and a measurement of $P_2^s(z)$, we can use equation (13) to construct $P_2^s(\bar{x}_{Hi})$. Since we assume that this latter quantity is known, we may tune z_r and β until the measured $P_2^s(\bar{x}_{Hi})$ matches the true one.

If a measurement of $P_2^{s,meas}(z)$ has Gaussian noise with an amplitude of σ, the likelihood of measuring this value is

$$\mathcal{L} = \prod_i \frac{1}{\sqrt{2\pi}\sigma} \exp\left[\frac{-\left(P_{2,i}^{s,meas} - P_{2,i}^{s,true}\right)^2}{2\sigma^2}\right], \quad (14)$$

where the product is calculated over all redshifts where there are measurements available. We are thus looking for the values of z_r and β that give rise to the $\bar{x}_{Hi}$ history that maximizes the likelihood.

Judging by Fig. 6, $P_2^s(\bar{x}_{Hi})$ can be assumed to be reasonably well-known, especially in the early stages of reionization. Here, we therefore only use the part of P_2^s where $\bar{x}_{Hi} \geq 0.75$, since the slope of $P_2^s(\bar{x}_{Hi})$ is very consistent from scenario to scenario. We take the values from the fiducial model light-cone to be the 'true' $P_2^s(\bar{x}_{Hi})$. More specifically, we use a linear fit to the values of $P_2^s(\bar{x}_{Hi})$ for $\bar{x}_{Hi} > 0.75$ plotted in Fig. 6 to be our $P_2^{s,true}$.

Fig. 11 shows the results of fitting the reionization history. $P_2^{s,meas}$ is here taken from our simulated reionization scenarios (see Fig. 6), and the noise σ is calculated as described in the previous section. In the left-hand panel we show the likelihood contours for LOFAR noise for 1000 and 3000 h of integration time and for SKA noise for 100 h. The crosses show the parameter values that maximize the likelihood, while the red circles show the true values, i.e. a fit of equation (13) to the true reionization history (since our simulations only go down to $\bar{x}_{Hi} \sim 0.2$, the value of z_r represents an extrapolation; c.f. Fig. 1). The error contours do not explicitly include the effects of sample variance.[5] The middle panel of Fig. 11 shows the reconstructed reionization histories corresponding to the best-fitting parameters in the left-hand panel.

The fact that the best-fitting values are very close to the true values for all reionization scenarios shows that the evolution of P_2^s can indeed be used as a robust measurement of the reionization history.

[5] The inherent non-Gaussianity in the EoR 21 cm signal can make the cosmic variance at these length scales deviate from its generally assumed Gaussian behaviour (Mondal et al. 2015a,b), increasing the uncertainties in the reconstruction of the EoR history.

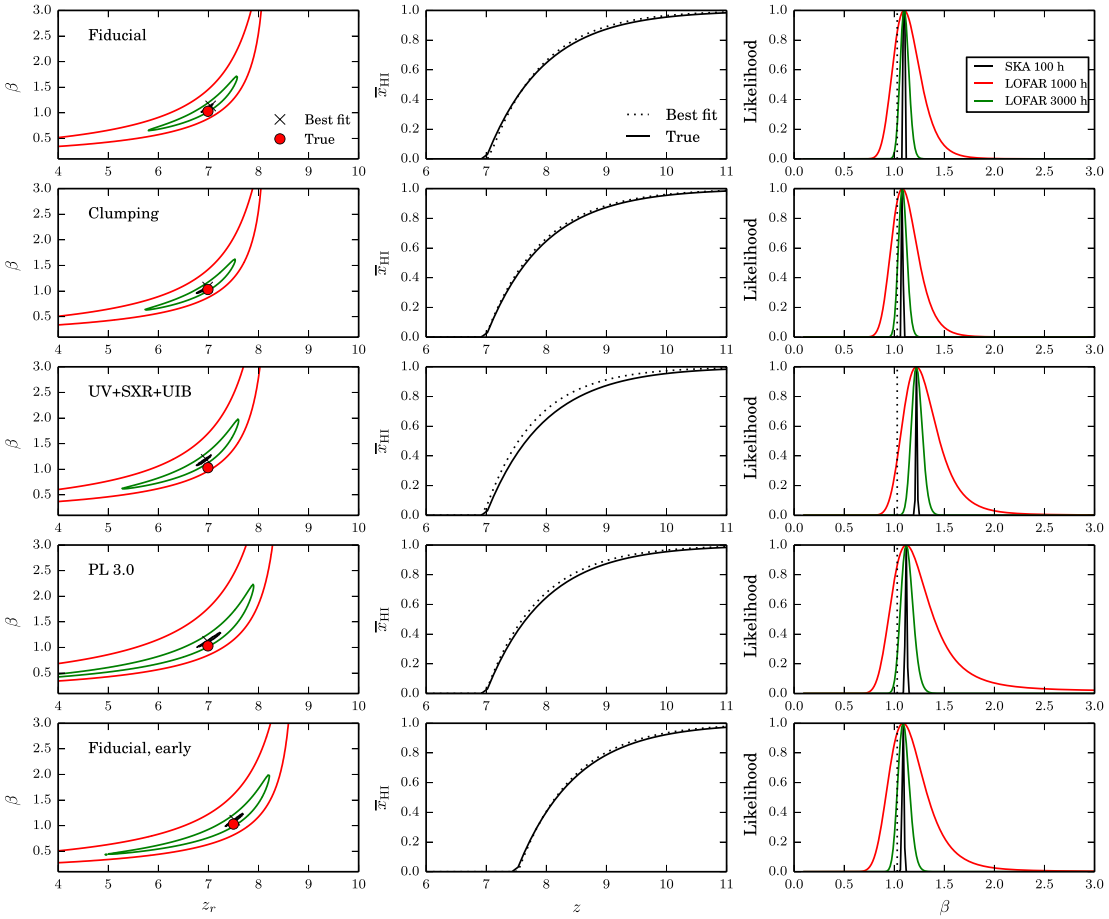

Figure 11. Fitting the reionization history to match the slope of P_2^s as a function of $\bar{x}_{\rm H\,I}$. Left-hand column: likelihood contours for 1000 and 3000-h integration time with LOFAR and 100 h of integration time with SKA, for different reionization scenarios. The contours are located at the value where the likelihood is a factor e^2 lower than the maximum value, corresponding to roughly 90 per cent of the full distribution. The crosses show the best-fitting values of the parameters $z_{\rm r}$ and β (in the absence of noise), and the red circles show the true values. Middle column: the reionization histories corresponding to the best-fitting values from the left-hand column, compared to the true histories. Right-hand column: same as the left-hand column, but assuming that $z_{\rm r}$ is known. The dotted vertical lines show the true values of β.

For LOFAR, it is clear that noise is an important obstacle. With 1000 h of integration time, we can only put rather loose constraints on the reionization history. After 3000 h, however, the constraints become much better. For the SKA, the noise is so low that even for 100-h integration time, the reionization history can be determined almost perfectly.

We also see that for our parametrization of the reionization history, there is quite a bit of degeneracy between the two parameters, as seen by the elongated likelihood contours. In a real-world scenario, it is likely that there will be some information available on one of the parameters. For example, $z_{\rm r}$ may be estimated by looking for the redshift when the spherically averaged power spectrum tends to zero. In the right-hand column of Fig. 11, we show the results of fitting only β, assuming that $z_{\rm r}$ is known. In this case, LOFAR measurements may be able to say something about the reionization history, or at least exclude meaningful regions of parameter space.

While all of our reionization scenarios are constructed to have very different topologies, they are also tuned to have the same reionization history. A widely accepted view is that the 21-cm power spectrum is much more sensitive to $\bar{x}_{\rm H\,I}$ than z (e.g. Iliev et al. 2012), and so we do not expect the reionization history to have a large effect on our results. Nevertheless, to test whether a different reionization history would change the shape of $P_2^s(\bar{x}_{\rm H\,I})$, we also constructed a scenario with the same source properties as the fiducial scenario, but with the source efficiencies increased, in order to produce an earlier reionization. The results for fitting the reionization history for this scenario are shown in the bottom row of Fig. 11, still using $P_2^s(\bar{x}_{\rm H\,I})$ from the fiducial scenario as the true value. While a full investigation of the effects of the exact reionization history is beyond the scope of this paper, it is clear from this test that a modest shift in the history has no significant effect on the results.

The analysis presented in this section is a proof-of-concept of the possibility of extracting the reionization history from the redshift-space anisotropy of the 21 cm signal. In actual radio-interferometric observations, the presence of residuals from foregrounds in the reduced 21 cm data can introduce further uncertainties in these estimations, which we have not accounted for.

6 SUMMARY AND CONCLUSIONS

The velocities of matter distort the 21 cm signal and cause the power spectrum to become anisotropic. The anisotropy depends on the cross-correlation between the density and the H I fields and therefore carries information both about the cosmology and about the properties of the sources of reionization. In this paper we have

explored a number of different reionization scenarios with different types of sources of ionizing photons in order to study the effect of the sources of reionization on the power spectrum anisotropy.

We find that the power spectrum anisotropy, as measured by the quadrupole moment of the power spectrum, P_2^s, as a function of global neutral fraction evolves in a very similar way for all reionization scenarios in which the sources and the matter distribution are strongly correlated. Only the most extreme scenarios, such as reionization driven by a uniform ionizing background or by very massive sources, show significant deviations from the others. Thus, P_2^s is not a sensitive tool for separating reionization scenarios. However, it can be used as a robust tracer of the reionization history.

Interferometers such as LOFAR or the SKA can only measure the fluctuations of the 21 cm signal, not the actual magnitude of the signal. Therefore, extracting the reionization history is not trivial, and can only be done by fitting a model to the observed data. Previous studies have suggested that looking for the peak in the spherically averaged power spectrum (e.g. McQuinn et al. 2007; Lidz et al. 2008; Barkana 2009; Iliev et al. 2012) or the variance (Patil et al. 2014) will give the mid-point of reionization. However, as seen in this paper and elsewhere (e.g. Iliev et al. 2006, 2007; Mellema et al. 2006; Watkinson et al. 2015), the spherically averaged power spectrum can in fact vary substantially depending on the properties of the sources of reionization. The quadrupole moment is much more model-independent, as long as the reionization topology is inside-out. This is likely to be the case, considering that the latest *Planck* results on the optical depth to Thomson scattering combined with observations of high-redshift galaxies strongly favour galaxies as the main driver of reionization (Bouwens et al. 2015).

We have shown that measuring the reionization history using the quadrupole moment works well for all reionization scenarios considered in this paper, except for the most extreme ones. For first-generation telescopes such as LOFAR, these types of measurements will be challenging due to the uncertainties imposed by the noise and foreground emission. However, it should be possible to use the power spectrum anisotropy to exclude certain reionization histories. In any case the anisotropy can be used to verify that the observed signal is indeed the 21 cm emission from the EoR. For the SKA, neither the noise uncertainty nor foregrounds will be an issue, and it will be possible to accurately measure the reionization history even with a relatively short integration time.

Of course, our treatment of observational effects here is simplified and does not take into account complications from, for example, the frequency dependence of the PSF, ionospheric effects or calibration errors. Nevertheless, it shows that the 21-cm power spectrum anisotropy due to the redshift-space distortions has the potential to be a powerful and nearly model-independent probe of the reionization history.

ACKNOWLEDGEMENTS

SM would like to thank Raghunath Ghara for useful discussions related to the effect of spin temperature fluctuations on the EoR 21 cm signal. The research described in this paper was supported by a grant from the Lennart and Alva Dahlmark Fund. GM is supported by Swedish Research Council project grant 2012-4144. The PRACE4LOFAR simulations were performed on the Curie system at TGCC under PRACE projects 2012061089 and 2014102339. This work was supported by the Science and Technology Facilities Council (grant no. ST/L000652/1). KKD would like to thank DST for support through the project SR/FTP/PS-119/2012 and the University Grant Commission (UGC), India for support through UGC-faculty recharge scheme (UGC-FRP) vide ref. no. F.4-5(137-FRP)/2014(BSR). VJ would like to thank the Netherlands Foundation for Scientific Research (NWO) for financial support through VENI grant 639.041.336. LVEK acknowledges the financial support from the European Research Council under ERC-Starting Grant FIRSTLIGHT – 258942.

REFERENCES

Ali S. S., Bharadwaj S., Chengalur J. N., 2008, MNRAS, 385, 2166
Ali Z. S. et al., 2015, ApJ, 809, 61
Alvarez M. A., Shapiro P. R., Ahn K., Iliev I. T., 2006, ApJ, 644, L101
Barkana R., 2009, MNRAS, 397, 1454
Barkana R., Loeb A., 2005, ApJ, 624, L65
Becker R. H. et al., 2001, AJ, 122, 2850
Becker G. D., Bolton J. S., Madau P., Pettini M., Ryan-Weber E. V., Venemans B. P., 2015, MNRAS, 447, 3402
Bharadwaj S., Ali S. S., 2004, MNRAS, 352, 142
Bharadwaj S., Ali S. S., 2005, MNRAS, 356, 1519
Bharadwaj S., Pandey S. K., 2005, MNRAS, 358, 968
Bouwens R. J., Illingworth G. D., Oesch P. A., Caruana J., Holwerda B., Smit R., Wilkins S., 2015, ApJ, 811, 140
Bowman J. D. et al., 2013, PASA, 30, 31
Chapman E. et al., 2013, MNRAS, 429, 165
Choudhury T. R., Haehnelt M. G., Regan J., 2009, MNRAS, 394, 960
Choudhury T. R., Puchwein E., Haehnelt M. G., Bolton J. S., 2015, MNRAS, 452, 261
Cole S., Fisher K. B., Weinberg D. H., 1995, MNRAS, 275, 515
Couchman H. M. P., Rees M. J., 1986, MNRAS, 221, 53
Datta K. K., Mellema G., Mao Y., Iliev I. T., Shapiro P. R., Ahn K., 2012, MNRAS, 424, 1877
Datta K. K., Jensen H., Majumdar S., Mellema G., Iliev I. T., Mao Y., Shapiro P. R., Ahn K., 2014, MNRAS, 442, 1491
Dewdney P., Turner W., Millenaar R., McCool R., Lazio J., Cornwell T., 2013, SKA1 System Baseline Design, Document number SKA-TEL-SKO-DD-001 Revision 1. SKA Organization, Cheshire, p. 1
Di Matteo T., Perna R., Abel T., Rees M. J., 2002, ApJ, 564, 576
Dijkstra M., Haiman Z., Rees M. J., Weinberg D. H., 2004, ApJ, 601, 666
Dillon J. S. et al., 2014, Phys. Rev. D, 89, 023002
Fan X. et al., 2003, AJ, 125, 1649
Fialkov A., Barkana R., Visbal E., 2014, Nature, 506, 197
Fialkov A., Barkana R., Cohen A., 2015, Phys. Rev. Lett., 114, 101303
Fragos T. et al., 2013, ApJ, 764, 41
Furlanetto S. R., Zaldarriaga M., Hernquist L., 2004, ApJ, 613, 1
Ghara R., Choudhury T. R., Datta K. K., 2015a, MNRAS, 447, 1806
Ghara R., Datta K. K., Choudhury T. R., 2015b, MNRAS, 453, 3143
Gnedin N. Y., 2000, ApJ, 542, 535
Goto T., Utsumi Y., Hattori T., Miyazaki S., Yamauchi C., 2011, MNRAS, 415, L1
Hamilton A. J. S., 1992, ApJ, 385, L5
Hamilton A. J. S., 1998, in Hamilton D., ed., Astrophysics and Space Science Library, Vol. 231, The Evolving Universe. Kluwer, Dordrecht, p. 185
Harnois-Déraps J., Pen U.-L., Iliev I. T., Merz H., Emberson J. D., Desjacques V., 2013, MNRAS, 436, 540
Iliev I. T., Mellema G., Pen U.-L., Merz H., Shapiro P. R., Alvarez M. A., 2006, MNRAS, 369, 1625
Iliev I. T., Mellema G., Shapiro P. R., Pen U.-L., 2007, MNRAS, 376, 534
Iliev I. T., Mellema G., Shapiro P. R., Pen U.-L., Mao Y., Koda J., Ahn K., 2012, MNRAS, 423, 2222
Jelić V. et al., 2008, MNRAS, 389, 1319
Jelić V., Zaroubi S., Labropoulos P., Bernardi G., de Bruyn A. G., Koopmans L. V. E., 2010, MNRAS, 409, 1647
Jelić V. et al., 2014, A&A, 568, A101
Jensen H. et al., 2013, MNRAS, 435, 460
Komatsu E. et al., 2009, ApJS, 180, 330
Komatsu E. et al., 2011, ApJS, 192, 18

Koopmans L. et al., 2015, Proceedings of Advancing Astrophysics with the Square Kilometre Array (AASKA14), The Cosmic Dawn and Epoch of Reionisation with SKA. SISSA, Trieste, PoS#1
Kuhlen M., Faucher-Giguère C.-A., 2012, MNRAS, 423, 862
Lidz A., Zahn O., McQuinn M., Zaldarriaga M., Hernquist L., 2008, ApJ, 680, 962
McQuinn M., 2012, MNRAS, 426, 1349
McQuinn M., Zahn O., Zaldarriaga M., Hernquist L., Furlanetto S. R., 2006, ApJ, 653, 815
McQuinn M., Lidz A., Zahn O., Dutta S., Hernquist L., Zaldarriaga M., 2007, MNRAS, 377, 1043
Madau P., Haardt F., Rees M. J., 1999, ApJ, 514, 648
Majumdar S., Bharadwaj S., Choudhury T. R., 2013, MNRAS, 434, 1978
Majumdar S., Mellema G., Datta K. K., Jensen H., Choudhury T. R., Bharadwaj S., Friedrich M. M., 2014, MNRAS, 443, 2843
Mao Y., Shapiro P. R., Mellema G., Iliev I. T., Koda J., Ahn K., 2012, MNRAS, 422, 926
Mellema G., Iliev I. T., Pen U.-L., Shapiro P. R., 2006, MNRAS, 372, 679
Mellema G. et al., 2013, Exp. Astron., 36, 235
Mellema G., Koopmans L., Shukla H., Datta K. K., Mesinger A., Majumdar S., 2015, Proceedings of Advancing Astrophysics with the Square Kilometre Array (AASKA14), HI tomographic imaging of the Cosmic Dawn and Epoch of Reionization with SKA. SISSA, Trieste, PoS#10
Merz H., Pen U.-L., Trac H., 2005, New Astron., 10, 393
Mesinger A., Furlanetto S., 2007, ApJ, 669, 663
Mesinger A., Furlanetto S., Cen R., 2011, MNRAS, 411, 955
Mesinger A., Ferrara A., Spiegel D. S., 2013, MNRAS, 431, 621
Mirabel I. F., Dijkstra M., Laurent P., Loeb A., Pritchard J. R., 2011, A&A, 528, A149
Mitra S., Ferrara A., Choudhury T. R., 2013, MNRAS, 428, L1
Mitra S., Choudhury T. R., Ferrara A., 2015, MNRAS, 454, L76
Mondal R., Bharadwaj S., Majumdar S., 2015a, MNRAS, preprint (arXiv:1508.00896)
Mondal R., Bharadwaj S., Majumdar S., Bera A., Acharyya A., 2015b, MNRAS, 449, L41
Morales M. F., 2005, ApJ, 619, 678
Okamoto T., Gao L., Theuns T., 2008, MNRAS, 390, 920
Paciga G. et al., 2013, MNRAS, 433, 639
Parsons A. R. et al., 2014, ApJ, 788, 106
Patil A. H. et al., 2014, MNRAS, 443, 1113
Planck Collaboration XIII 2015, preprint (arXiv:1502.01589)
Pober J. C. et al., 2014, ApJ, 782, 66
Robertson B. E., Ellis R. S., Furlanetto S. R., Dunlop J. S., 2015, ApJ, 802, L19
Santos M. G., Ferramacho L., Silva M. B., Amblard A., Cooray A., 2010, MNRAS, 406, 2421
Shapiro P. R., Mao Y., Iliev I. T., Mellema G., Datta K. K., Ahn K., Koda J., 2013, Phys. Rev. Lett., 110, 151301
Sobacchi E., Mesinger A., 2014, MNRAS, 440, 1662
Songaila A., Cowie L. L., 2010, ApJ, 721, 1448
Tingay S. J. et al., 2013, PASA, 30, 7
van Haarlem M. P. et al., 2013, A&A, 556, A2
Wang J. et al., 2013, ApJ, 763, 90
Watkinson C. A., Pritchard J. R., 2014, MNRAS, 443, 3090
Watkinson C. A., Mesinger A., Pritchard J. R., Sobacchi E., 2015, MNRAS, 449, 3202
White R. L., Becker R. H., Fan X., Strauss M. A., 2003, AJ, 126, 1
Yatawatta S. et al., 2013, A&A, 550, A136
Zahn O., Lidz A., McQuinn M., Dutta S., Hernquist L., Zaldarriaga M., Furlanetto S. R., 2007, ApJ, 654, 12

APPENDIX A: BEHAVIOUR OF THE QUADRUPOLE MOMENT

The similarity in the behaviour of the quadrupole moment, P_2^s (Fig. 6), estimated for different reionization scenarios may appear unintuitive. However, it can be explained using the quasi-linear model (equation 7), where the major contribution in the evolution of P_2^s has been ascribed to the evolution of $P_{\rho_{\rm Hi},\rho_{\rm M}}$ (Fig. 7).

The cross-power spectrum between two fields, defined in Fourier space as $X = Ae^{i\theta}$ and $Y = Be^{i\phi}$, will be $P_{XY} = {\rm Re}(X^*Y) = |A||B|\cos(\phi - \theta)$. Thus the cross-power spectrum between the matter and the H I fields ($P_{\rho_{\rm Hi},\rho_{\rm M}}$), is essentially a product of three quantities: the amplitudes of the matter density fluctuations and the H I density fluctuations and the cosine of the phase difference between these two fields. Since the matter density fluctuations are the same for all our reionization scenarios, this means that the differences in $P_{\rho_{\rm Hi},\rho_{\rm M}}$ will be solely due to the differences in the amplitude of their H I density fluctuations and its relative phase with the matter density field.

The top panel of Fig. A1 shows the evolution of the cosine of this phase difference for different reionization scenarios estimated through the cross-correlation coefficient $r_{\rho_{\rm Hi},\rho_{\rm M}}(k) = P_{\rho_{\rm Hi},\rho_{\rm M}}(k)/\sqrt{P_{\rho_{\rm Hi},\rho_{\rm Hi}}(k)P_{\rho_{\rm M},\rho_{\rm M}}(k)}$. An obvious observation from Fig. A1, is that the evolution of $r_{\rho_{\rm Hi},\rho_{\rm M}}$ is very similar in all of the reionization scenarios, except for the UIB dominated scenario. This is because as long as the spatial distribution of the major reionization sources follows the underlying matter distribution, the relative phase between the H I and the matter density fields remains approximately the same and also evolves similarly. In other words, $r_{\rho_{\rm Hi},\rho_{\rm M}}$ evolves similarly as long the reionization is inside-out in nature.

The bottom panel of Fig. A1 shows the evolution of the H I density power spectrum $P_{\rho_{\rm Hi},\rho_{\rm Hi}}$, which measures the amplitude of fluctuations in the H I field. The square root of $P_{\rho_{\rm Hi},\rho_{\rm Hi}}$ is the other quantity effectively contributing to the evolution of $P_{\rho_{\rm Hi},\rho_{\rm M}}$. It is evident from this figure that the amplitude and the location of the peak in $P_{\rho_{\rm Hi},\rho_{\rm Hi}}$ is significantly different for different reionization scenarios as it is more susceptible to the H I topology. In the cross-power spectrum, however, it gets tuned by the phase difference ($r_{\rho_{\rm Hi},\rho_{\rm M}}$) term. This is what makes the contribution from $P_{\rho_{\rm Hi},\rho_{\rm M}}$ in P_2^s similar in most of the reionization scenarios.

According to the quasi-linear model (equation 6), P_0^s also contains a contribution from $P_{\rho_{\rm Hi},\rho_{\rm M}}$, but in addition to that it also contains contribution from the power spectrum of the H I field, $P_{\rho_{\rm Hi},\rho_{\rm Hi}}$, which as described before, depends only on the amplitude of the H I fluctuations and not on its relative phase with density field. The contribution from $P_{\rho_{\rm Hi},\rho_{\rm Hi}}$ makes the monopole moment P_0^s more sensitive to the H I topology (or the H II bubble size distribution) and thus more dependent on the specific reionization scenario (a visual comparison of Fig. 6 with the bottom panel of Fig. A1 further strengthens this argument). Because of this the P_2^s is a more robust measure of the reionization history than P_0^s.

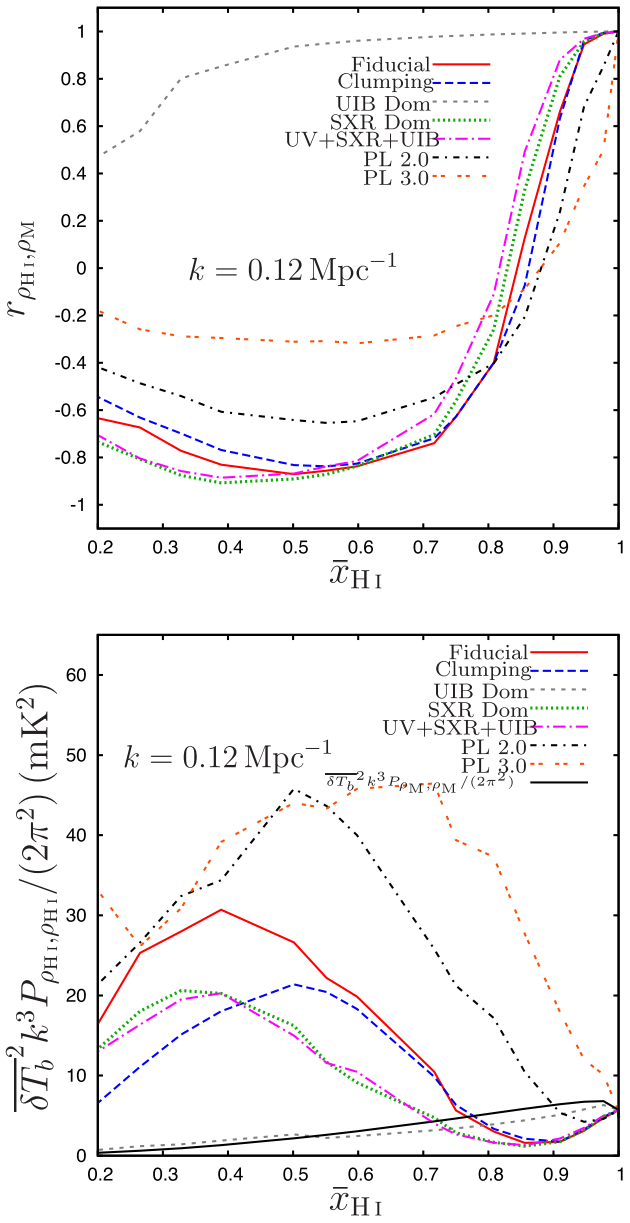

Figure A1. The top and the bottom panels show the cross-correlation coefficient (or the cosine of the relative phase) between the matter and the H I density fields, and the H I density fluctuation power spectrum $P_{\rho_{\mathrm{H\,I}},\rho_{\mathrm{H\,I}}}$, respectively, for all of our reionization scenarios, as a function of the global neutral fraction at $k = 0.12$ Mpc^{-1}.

This paper has been typeset from a TEX/LATEX file prepared by the author.